URSI GASS 2023, Sapporo, Japan, 19 – 26 August 2023

A Comparison of Non-corrected Planar and Spherical Near-Field Scanning For Absorbed Power Density Evaluation Using Inverse Source Technique

Rasyidah Hanan Binti Mohd Baharin*(1), Kensuke Sasaki(1), and Tomoaki Nagaoka(1)
(1) Radio Research Institute, National Institute of Infomation and Communications Technology, Koganei, Japan;
e-mail: {rasyidah, k_sasaki, nagaoka}@nict.go.jp

Abstract

A comparison of absorbed power density (APD) evaluation using a regularized source reconstruction/inverse source method by planar and spherical near-field sampling was studied for a horn antenna at a millimeter-wave frequency of 28 GHz. The results have shown that the non-corrected planar near-field scanning for the proposed inverse source method could calculate a reasonably accurate peak spatial APD compared to that of a spherical one, in addition to the significantly reduced number of sampling points. The calculated APD using measured planar near field was also presented as validation.

1 Introduction

The epithelial/absorbed power density (APD) in W m^{-2} has been determined as the dosimetric reference limit or basic restrictions for human exposure above 6 GHz [1, 2], its poynting vector definition given as Eq. (1), where **E**, **H**, and A are electric field (V m^{-1}), magnetic field (A m^{-1}), and averaging area (m), respectively.

$$\mathrm{APD} = \iint_A \mathrm{Re}[\mathbf{E} \times \mathbf{H}^*] \cdot ds/A \tag{1}$$

As there are no current set standards on the methodology and procedures, the development of an APD measurement method becomes an active research in the scientific community focusing on radiation protection by electromagnetic fields. Recently, there were some attempts to develop APD prototype by extension of conventional specific absorption rate (SAR) measurement system [3] and also by plane wave spectrum method [4]. Nevertheless, the measurement at higher frequencies above 10 GHz still proves to be a challenging subject, especially considering the scattering of high-loss phantom. For this reason, we consider the APD measurement prototype with the inverse source method (ISM) approach [5]. The basis of ISM-based APD assessment is utilizing a probe's surface field measurement of a device under test (DUT) irradiating a lossless (technically very low-loss) phantom. Then, the equivalent electric currents on the surface of the phantom are reconstructed for calculating the spatial averaged peak APD (psAPD) for the high-loss phantom.

In order to obtain the surface field measurement in millimeter-wave (MMW), the over-the-air (OTA) measurement method becomes the only viable method. However, the spherical near-field (SNF) sampling with OTA which is generally the most accurate technique to characterize the radiation of DUT are not easily available commercially within the 5G domain. In addition, the sampling criterion for higher frequency results in longer sampling time and ultimately more expensive computation. Therefore, utilizing the existing OTA based on planar-near field (PNF) is the more viable option for 5G devices. In this paper, to ensure that the PNF is a suitable near-field sampling method for our proposed method, the APD reconstruction based on ISM is compared between PNF and SNF at a frequency of 28 GHz.

2 Inverse Source Method for APD

The ISM in electromagnetics (EM), or sometimes dubbed as "source reconstruction" is an advantageous noninvasive/non-destructive approach for APD assessment, yet relatively unexplored for multiple reasons. The major disadvantage is the inherently ill-conditioned nature of the matrix when considering high permittivity objects. ISM problems involving a scattering on non-metallic surfaces (dielectric, bio-equivalent phantom) are generally solving rectangular matrices of $\mathbf{b} = \mathbf{Ax}$ where unique solutions do not exist on the boundaries of the medium. However, with appropriate preconditioning, the system of equations can be transformed into a square matrix and solved iteratively using solvers such as least-square approximation.

A DUT radiating in free space, simplified, is shown in Eq. (2) where **E** at observation point of (**r**) at different measurement points is $[E_1, \cdots, E_m]^\mathsf{T}$, and the unknown coefficients of source currents $\mathcal{X}(\mathbf{J},\mathbf{M})$ are $[X_1 \cdots, X_n]^\mathsf{T}$. However, In this study, since the coefficient matrices are the unknown variable, the matrix-vector product becomes more computationally expensive and therefore the generalized minimal residual method (GMRES) is preferable and used for the iterative solver.

$$\begin{bmatrix} E_1 \\ \vdots \\ E_m \end{bmatrix} = \begin{bmatrix} A_{j,11} & \cdots & A_{j,1n} \\ \vdots & \ddots & \vdots \\ A_{j,m1} & \cdots & A_{j,mn} \end{bmatrix} \begin{bmatrix} X_1 \\ \vdots \\ X_n \end{bmatrix} \tag{2}$$

For DUT irradiating a phantom, a scattering problem arises for two surfaces, $\mathbf{J}_1, \mathbf{M}_1$ (on equivalent surface of DUT, S_{DUT}) and $\mathbf{J}_2, \mathbf{M}_2$ (on equivalent surface of phantom, S_{pha}). The observed electric field at sampling points $\mathbf{E}(\mathbf{r})$, of SNF (on S_{sp}) or PNF (on S_{pl}) is given as,

$$\begin{aligned}\mathbf{E}(\mathbf{r}) &= (\mathbf{E}_{dir} + \mathbf{E}_{sca}) \quad ;\mathbf{r} \\ &= (-\mathrm{L}^{k_0}\eta_0(\mathbf{J}_1) + \mathrm{K}^{k_0}(\mathbf{M}_1) - \mathrm{L}^{k_0}\eta_0(\mathbf{J}_2) + \mathrm{K}^{k_0}(\mathbf{M}_2)) \;;\mathbf{r}\end{aligned} \tag{3}$$

where $\mathbf{E}_{dir}$ is the direct wave propagation and $\mathbf{E}_{sca}$ is scattered field. The superscript k_n is the wavenumber while subscript η_n is wave impedance where $n = 0$ and phantom $n = 1$ are for regions free space and phantom, respectively. PMCHW formulation is the approach taken to build the matrices corresponding $\mathbf{J}_{1,2}$, $\mathbf{M}_{1,2}$ [6]. To obtain $\mathbf{E}$ with respect to Eq. (1), the observed fields at sampling points can be assumed as the exterior fields to the phantom surface. Based on the surface equivalent theory, thus the corresponding internal electric fields of the phantom are given as following.

$$\mathbf{E} = \mathrm{L}^{k_1}\eta_1(\mathbf{J}_2) + \mathrm{K}^{k_1}(\mathbf{M}_2) \tag{4}$$

Taking the various conditions into consideration, the geometry of the problem is shown in Figure 1. The d_p, d_r, and t are distances/thickness of DUT-phantom-probe, meanwhile (R, θ, ϕ) and (x, y) are the typical nomenclatures of the spherical and planar coordinates, respectively.

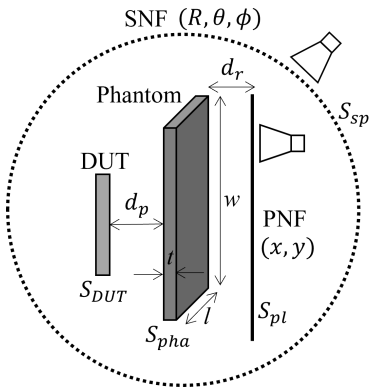

Figure 1. Schematic representation of PNF and SNF for APD reconstruction.

3 Validation Procedure

The low-loss phantom is represented by a polymer resin, Polyphenylene ether (PPE), specified as $\varepsilon_r = 10.21$ and tan $\delta = 0.006$ with dimension $200 \times 200 \times 5$ mm ($l \times w \times t$) (CS-3396, RISHO Kogyo Co. Ltd.). PPE is typically used as an antenna substrate in 5G communication devices as it is a material that exhibits stable dielectric properties over a wide frequency and temperature range. For this reason, we consider the PPE as the suitable candidate for the low-loss phantom. For a high-loss phantom, the average of wet and dry skin tissue was calculated $\varepsilon_r = 17.6$, $\sigma = 26$ at 28 GHz [7]. For the DUT, a standard gain conical horn antenna was deployed (Ka-band, QWH series, QuinStar Technology, Inc.) with input power of 1 mW. The equivalent surface of the DUT is represented at the horn's aperture, a closed surface of 5 mm $\times$ 5 mm with a thickness of 0.05 mm. The phantom is placed from a distance of 5 mm from the aperture of the antenna.

The validation procedure with measurement is only performed with the PNF due to the availability of the measurement facility. The measurement setup is shown as following Figure 2. A polystyrene plate is perforated with a square hole in the middle to radiate directly to the surface of the phantom. The probe is a WR-28 open-ended waveguide antenna (AOEWP-08E, Elmika UAB). For PNF, it is preferable for the separation distance between DUT and probe, $d_{rx} = d_p + t + d_r$ is greater than several λs to minimize coupling effects and multiple reflections from the DUT to the receiving probe. If this criterion is fulfilled, the minimum increment of sampling can be simplified as shown Eq. (5).

$$\Delta x = \Delta y = \frac{\lambda}{2} \tag{5}$$

Therefore, the increment of scanning for both x, y is set as 5mm for the selected $d_{rx} = 60$ mm (5.7λ). This brings the sampling points of PNF to $N = 41 \times 41$ points. In the initial test, We measured the PNF with a scanning area of the same dimension as that of the D_{max}, or the largest dimension of the object in the geometry of the problem.

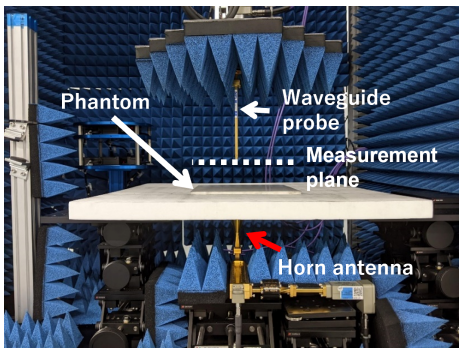

Figure 2. Measurement setup of PNF scanning.

The calculated APD was spatially averaged over a square area of 4 cm^2 which is the exposure metric specified in IEEE C95.1 standard [1] and ICNIRP guideline [2]. The results are shown in Figure 3. The reference is calculated by utilizing the currents' output file generated from FEKO, a commercial EM simulator. The psAPD of Figure 3(a) returns a very small error of -0.19 dB or approximately corresponding to 4.3% error compared to psAPD of reference of Figure 3(c). Meanwhile, psAPD of (Figure 3(b)) returns a reasonable deviation of -1.14 dB, corresponding to error of 23.0%.

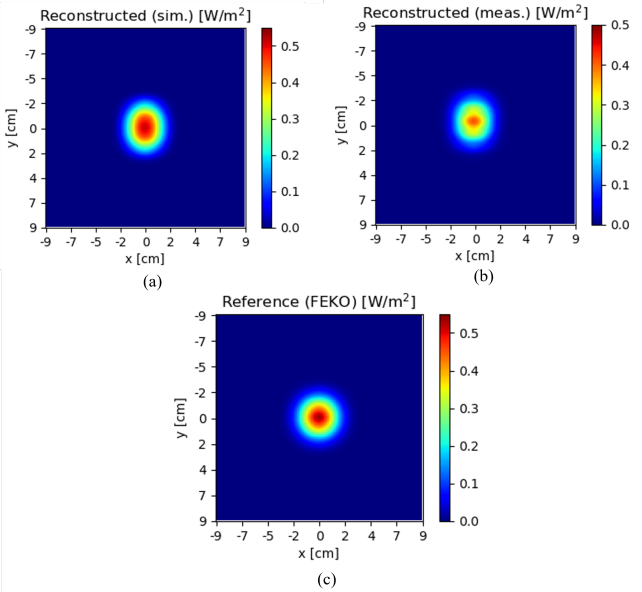

Figure 3. The spatial-averaged APD, (a) Reconstructed using simulated PNF generated by FEKO (b) Reconstructed using measured PNF (c) Reference, calculated directly with surface currents generated by FEKO.

4 Discussion

In the previous section, a satisfactory reconstruction of APD was obtained using PNF scanning. Let us compare the results with the reconstruction using SNF. The distinct characteristic of SNF scanning is the full enclosure of geometry by the minimum measurement sphere. This theoretically ensures that the probe is always pointing at DUT and all radiations will be measured, with a reduction of scattered fields and noise influence [9]. According to the sampling theory, the minimum step for angular sampling (in radian) is calculated as following equation [10, 11].

$$\Delta\theta = \Delta\phi = \frac{\lambda}{2(\frac{D_{max}}{2}) + \lambda} \tag{6}$$

The sampling interval for SNF is selected as equiangular, $\Delta\theta = \Delta\phi = 1^\circ$, corresponding to $N = 181 \times 361$ points. The radius of the full-sphere enclosing the whole problem is $R = 0.15$ m (14λ). There are some cases where hemisphere scanning can be utilized to effectively halve the sampling time and overcome certain mechanical arm limitations with regards to θ or ϕ, but it is not to be considered in this paper. The other parameters including the phantom and antenna are kept the same as that of Section 3.

The calculated APD is shown in Figure 4. The psAPD of reconstruction using SNF agrees extremely well with reference. The overall results are summarized in Table 1. However, even though the reconstruction using SNF is more accurate than PNF, the sampling points of PNF are much lower compared to that of SNF ($N = 1681$ points and $N = 65,341$ points, respectively) and we could obtain

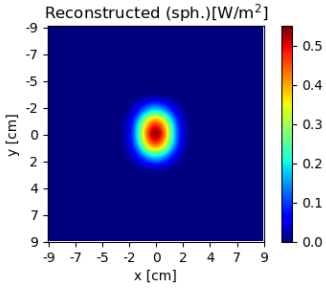

Figure 4. The spatial-averaged APD reconstructed using simulated SNF.

comparable results, therefore we have confirmed that PNF can be used confidently as a sampling technique for APD measurement method.

Table 1. Summary of results.

Units	Spherical	Planar		Reference
	Sim.	Sim.	Meas.	Sim.
psAPD, W/m^2	0.539	0.513	0.412	0.535 W/m^2
Difference, dB	0.032	-0.189	-1.137	
Difference,%	0.007	4.3	23.0	

5 Conclusion

In this paper, we compared the results of non-corrected PNF and SNF for calculating the APD using the regularized inverse source method. The results have shown that PNF sampling was able to obtain data comparably to that of SNF with computational simulation. The result was also validated using the measured results of PNF, which is a novelty in frequency of 28 GHz. We plan to further validate the measurement results using various conditions.

Acknowledgements

This work was supported by the Ministry of Internal Affairs and Communications, Japan, under Grant Number JPMI10001.

References

[1] "IEEE Standard for Safety Levels with Respect to Human Exposure to Electric, Magnetic, and Electromagnetic Fields, 0 Hz to 300 GHz - Redline" in *IEEE Std C95.1-2019 (Revision of IEEE Std C95.1-2005/ Incorporates IEEE Std C95.1-2019/Cor 1-2019)* - Redline , pp.1-679, 4 Oct. 2019.

[2] "Guidelines for Limiting Exposure to Electromagnetic Fields (100 kHz to 300 GHz)," *International Commission on Non-Ionizing Radiation Protection (ICNIRP)*, Health Phys, May 2020, **118**, 5, pp. 483-524, doi: 10.1097/HP.0000000000001210.

[3] T. Samaras et. al, “Compliance Assessment of the Epithelial or Absorbed Power Density Below 10GHz Using SAR Measurement Systems,” in *Bioelectromagnetics*, **42**, 6, pp. 484-490, September 2021, doi:10.1002/bem.22355.

[4] S. F. Jafari et. al, “Absorbed/Epithelial Power Density Assessment Using Plane-Wave Spectrum Method From Inside the Skin Tissue Above 6 GHz,” in *IEEE Transactions on Instrumentation and Measurement*, **71**, pp. 1-8, April 2022, Art no. 5501708, doi: 10.1109/TIM.2022.3167770.

[5] S. Omi et. al, “Performance Analysis of Incident Power Density Evaluation by Inverse Source Method for Compliance Assessment at Quasi-Millimeter and Millimeter Wave Bands” in *IEEE Transactions on Electromagnetic Compatibility*, **63**, no. 5, pp. 1649-1657, Oct. 2021, doi: 10.1109/TEMC.2021.3100575.

[6] X. Q. Sheng et. al, “Solution of combined-field integral equation using multilevel fast multipole algorithm for scattering by homogeneous bodies” *IEEE Trans. Antennas Propag.*, **46**, 11, pp. 1718–1726, 1998.

[7] D.Andreuccetti, R.Fossi and C.Petrucci: An Internet resource for the calculation of the dielectric properties of body tissues in the frequency range 10 Hz - 100 GHz. IFAC-CNR, Florence (Italy), 1997. Based on data published by C.Gabriel et al. in 1996. [Online]. Available: http://niremf.ifac.cnr.it/tissprop/

[8] "IEC/IEEE International Standard - Measurement procedure for the assessment of specific absorption rate of human exposure to radio frequency fields from hand-held and body-mounted wireless communication devices – Part 1528: Human models, instrumentation, and procedures (Frequency range of 4 MHz to 10 GHz)," in *IEC/IEEE 62209-1528:2020*, vol., no., pp.1-284, 19 Oct. 2020, doi: 10.1109/IEEESTD.2020.9231298.

[9] O. Breinbjerg, "Spherical near-field antenna measurements — The most accurate antenna measurement technique," 2016 IEEE International Symposium on Antennas and Propagation (APSURSI), 2016, pp. 1019-1020, doi: 10.1109/APS.2016.7696217.

[10] A. Yaghjian, “An overview of near-field antenna measurements,”*IEEE Transactions on Antennas and Propagation*, **34**, 1, pp. 30-45, January 1986, doi: 10.1109/TAP.1986.1143727.

[11] J. E. Hansen, “Spherical Near-field Antenna Measurements”, 1988, The Institution of Engineering and Technology, London, United Kingdom.